A Comprehensive Evaluation of Tempering Kinetics on 3rd Generation Advanced High Strength Steels

Dileep Chandran Ramachandran [a,*], Abdelbaset R.H. Midawi [a], Mohammed Shojaee [a], Oleksii Sherepenko [a], Hassan Ghassemi-Armaki [b], Elliot Biro [a]

[a] Centre for Advanced Materials Joining, Department of Mechanical & Mechatronics Engineering, University of Waterloo, Waterloo, Ontario N2L 3G1, Canada

[b] Manufacturing Systems Research Laboratory, Global Research and Development, General Motors LLC, Warren, MI 48092, USA

* Corresponding author: Dileep Chandran Ramachandran

Centre for Advanced Materials Joining,

Department of Mechanical & Mechatronics Engineering,

University of Waterloo,

Waterloo, Ontario,

Canada N2L 3G1

E-mail: dcramachandran@uwaterloo.ca

Abstract

Emerging third-generation advanced high strength steels (3G AHSS) grades are being increasingly considered for autobody applications owing to their complex microstructures providing an excellent combination of strength and ductility. When welded with RSW, 3G AHSS such as 3G 1180 and 3G 980, exhibits a solid-state transformation in the sub-critical-heat-affected-zone (SCHAZ) due to the heat generated during the RSW process. The resulting changes in microstructure can affect the mechanical properties of the material within and around the spot welds and thereby influence the performance of welded components in case of a vehicle crash event. To study metallurgical transformations in the SCHAZ during the RSW process, 3G 1180 and 3G 980, and a reference martensitic press hardened steel, PHS 1500, were selected. These materials were subjected to isothermal tempering experiments at temperatures ranging between 350°C and 650°C and different tempering times from 0.2s to 24hr. It was shown that the Hollomon-Jaffe model accurately describes the tempering kinetics of 3G 1180 and PHS 1500 but does not predict the transformation processes in the SCHAZ of 3G 980. The PHS 1500 and 3G 1180 showed softening (tempering) for all combinations of investigated tempering times and temperatures due to the decomposition of martensite. In contrast, the 3G 980 showed a combination of softening by the formation of martensite and secondary ferrite combined with secondary hardening due to the formation of fine M_2C typed plate-like carbides. Furthermore, during long tempering, the M_2C particles dissolve into the matrix and were replaced by cementite particles in 3G 980.

Keywords: 3G Advanced High Strength Steels, Welding, Microstructure, Subcritical Heat Affected Zone, Tempering, Softening, Secondary hardening.

Introduction

The simultaneous demand to improve vehicle crashworthiness and fuel economy have resulted in employing advanced high-strength steels (AHSS) within vehicle body structure components [1–4]. Further use of AHSS has been shown as an effective solution for reducing the weight of the steel in body-in-white structures by reducing the steel sheet thickness. As a result, newer members of third-generation AHSS (3G AHSS), such as quenched and partitioned (Q&P) steels, are replacing the conventional steels in an attempt to respond to the constant requirement of higher safety standards and lower greenhouse emissions [5–7].

3G AHSS are known for their exceptional combination of strength and ductility. The high strength and high ductility of these steels are attributed to the various micro constituents within their microstructure. Phases such as retained austenite, martensite, bainite, and ferrite are commonly reported constituents in 3G AHSS [7–10]. The attractive properties of 3G AHSS make them a desirable option for automotive applications. However, these properties are affected by welding during vehicle assembly. Resistance spot welding (RSW) is the predominant welding process used in automotive assembly lines [11,12]. It has been reported that the rapid heating and cooling inherent in the RSW process alters the properties of the heat-affected zone (HAZ), and fusion zone (FZ) [13]. Although the combination of micro constituents such as martensite, bainite, ferrite, and retained austenite are responsible for the favorable mechanical properties of 3G AHSS, subjecting these advanced steels to the RSW heating cycle can decompose the martensite phase and induce other microstructural changes such as dissolution of carbides in ferrite, reduced dislocation density in ferrite, etc. It is reported that martensite starts decomposing when heated above approximately 80 °C and below A_{C1} temperature to form ferrite and cementite (tempered martensite), which have a lower hardness than the initial martensite. This phenomenon is generally referred to as HAZ softening. [14,15]. HAZ softening can lead to strain localization and premature failure along the subcritical HAZ (SCHAZ) at stresses below the base material's ultimate tensile strength thereby deteriorating the load-bearing capacity of the joints [16–19].

Softening is a critical phenomenon that occurs in the SCHAZ of resistance spot welded AHSS, and has been acknowledged by numerous studies so far [15,20–25]. Martensitic tempering, which is responsible for HAZ softening, is comprised of three main stages [26–32]. The first stage of tempering occurs at a temperature between 80 °C and 180 °C and includes segregation and redistribution of carbon atoms at lattice defects. In high C martensite (>0.61 wt.% C), transitional ε-carbides ($Fe_{2.4}C$) also form during this stage [30,32]. In stage two of tempering in conventional AHSS includes the transition of retained austenite (which is trapped between the laths of martensite) to ferrite and cementite at a temperature range of 200 °C to 300 °C [29,31]. During the third stage, the segregated carbon and transitional carbide transform to cementite at a temperature range of 250 °C to 350 °C [28]. Cementite precipitation and growth, ferrite recrystallization, and grain growth are the known processes happening simultaneously within that temperature range occurring in the SCHAZ which is below A_{C1} temperature [33]. The combination of tempering temperature and the tempering time determines the extent of the tempering phenomenon. Moreover, the material chemistry and initial microstructure are also other key factors that affect the tempering phenomenon.

Xia *et al.* [34] reported that the maximum potential softening in dual-phase (DP) steel has a linear relationship with the initial martensitic volume fraction. This was attributed to the transformation of martensite into tempered martensite (TM), which reduces the overall hardness of the SCHAZ. Furthermore, the presence of high-carbon martensite in the material increases softening since the high-carbon martensite promotes cementite formation [21]. Moreover, the presence of carbide-forming elements such as Cr and Mo slows down the softening process by retarding the cementite precipitation or growth within the TM[35]. Secondary hardening has also been reported for certain steels, along with the softening. Saha *et al.* [28] reported that secondary hardening in a bainite-containing DP 780 steel, was due to the transformation of pre-existed carbides such as Fe_3C and TiC into needle-shaped M_2C and plate-shaped M_4C_3. In other words, the preexisted carbides acted as a carbon source when dissolved in the matrix microstructure. Another work conducted by Zhang *et al*. [36] investigated the secondary hardening in ultra-high-strength stainless steel

with 0.20C–14.2Co–5.7Ni–9.8Cr–2.0Mo–0.3V. They pointed out that the precipitation of fine M_2C particles, approximately 20 nm in size, segregated in the martensitic lath and contributed to the secondary hardening behavior.

Although a considerable amount of work has investigated the mechanism behind SCHAZ softening in the previous generation of AHSS, no systematic study has examined the SCHAZ softening and hardening phenomena in the third generation AHSS. A review of the available literature reveals that in 3G AHSS, the softening and secondary hardening processes may occur simultaneously, and the microstructural progression and conclusion of the processes are not clear. Hence, this study focuses on evaluating the SCHAZ of two 3G steels (3G 1180 and 3G 980) by isothermal tempering experiments. A wide matrix of time and temperature was taken into experimentation, and the results are correlated with electron micrographs to explain both softening and hardening behavior within the SCHAZ of 3G 1180 and 3G 980 during the RSW process.

Materials and methods

The present study examines two uncoated 1.4 mm thick 3G 980, and 3G 1180 with ultimate tensile strength (UTS) of 980 and 1180 MPa, respectively, and one Al-Si coated 1.4 mm thick press hardened steel (PHS) with UTS of 1500 MPa (PHS 1500). The PHS 1500 was included in this study as a basis for tempering behavior comparison between 3G 1180, and 3G 980 with previous generations of AHSS. The carbon equivalent (C_{eq}) of the investigated steels was calculated using the formula proposed by Yurioka *et al.* [37] (see **Error! Reference source not found.**), and their values are 0.64, 0.69, and 0.48 for 3G 980, 3G 1180, and PHS 1500, respectively as shown *Table 1*. The mechanical properties of the base material (BM) steels were extracted from a standard tension test interfaced with the digital image correlation (DIC) technique, and the outcomes are summarized in *Table 2*.

$$C_{eq} = C + A(C).\{\frac{Si}{24} + \frac{Mn}{6} + \frac{Cu}{20} + \frac{Ni}{20} + \frac{Cr+Mo+Nb+V}{5} + 5B\} \quad \text{Equation 1}$$

$$\text{Where } A(c) = 0.75 + 0.25\tanh\{20(C - 0.12)\} \quad \text{Equation 2}$$

Table 1: Chemical composition and C_{eq} of the investigated steels

	C	Mn + Si	Ti+Mo+V+Nb	C_{eq}
3G 980	0.22	3.62	> 0.012	0.64
3G 1180	0.17	4.13	> 0.030	0.69
PHS 1500	0.22	1.42	> 0.037	0.48

Table 2: Mechanical properties of the investigated steels

Material	YS (MPa)	UTS (MPa)	Total elongation (%)	Hardness ($HV_{0.2}$)
3G 980	606 ± 8	1002 ± 8	28.1 ± 1.0	289 ± 3.7
3G 1180	993 ± 17	1230 ± 4	16.5 ± 0.4	397 ± 3.0
PHS 1500	1228 ± 16	1623 ± 16	6.9 ± 0.6	494 ± 1.4

RSW was performed using a medium frequency direct current (MFDC) RSW robot with a C-type spot welding gun interfaced with a Rexroth Bosch weld controller. Group A, class II, Cu-Cr dome-shaped electrodes with a flat face diameter of 7 mm were used for welding. The RSW process parameters were chosen according to the guidelines of AWS D8.9 standard [38] and are reported in Table 3. More details regarding the RSW process can be found in previous works [1,39].

Table 3: RSW process parameters utilized in this study

Electrode Force (kN)	Squeeze time (ms)	Total weld time (ms)	Hold time (ms)	Number of pulses	Cool time between pulses (ms)
4.9	167	334	167	2	34

All rapid tempering heat treatments were carried out using a Gleeble 3500 thermo-mechanical simulator. The gleeble samples were machined with their gauge length parallel to the rolling direction of the sheets, and the corresponding sample geometry is shown in *Figure 1a.* The samples were sectioned for metallographic and hardness analysis. The sectioning plane and indentation patterns are schematically shown in *Figure 1b and c*, respectively. The average heating and cooling rates used in the experiments were approximately 1000 °C/s.

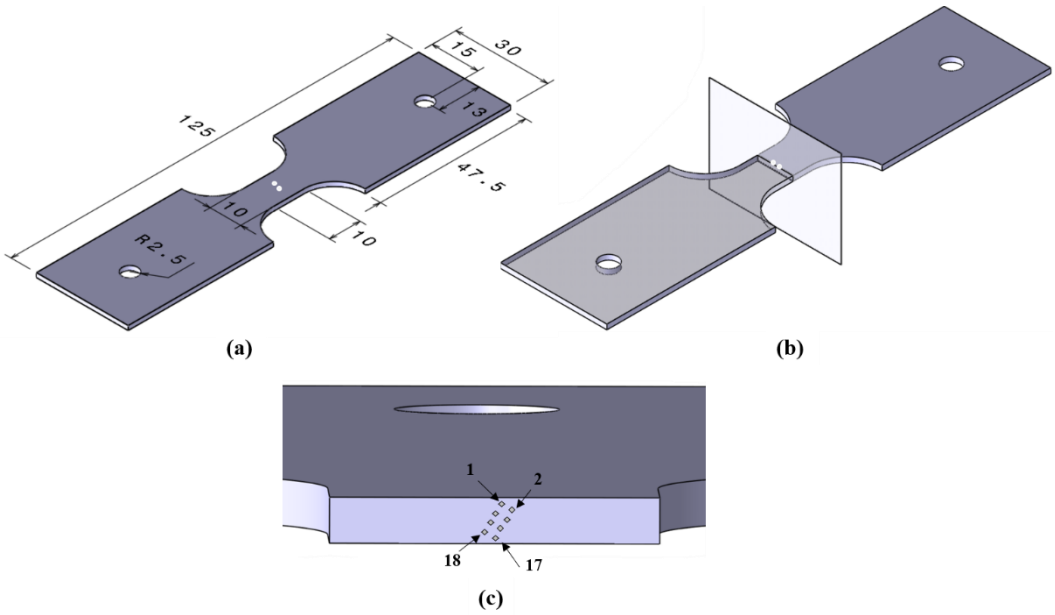


Figure 1: Schematic representation of (a) sample used for the gleeble thermomechanical simulations, (b) the sectioning plane for metallographic analysis, and (c) representation of the hardness analysis (all dimensions are in mm)

The detailed thermal profile used in the experiment for 0.2 s holding time at 650 °C is shown in *Figure 2a*. The sample temperature slightly varies from the target temperature (see *Figure 2b*) only in the lower holding time (0.2 s to ~1 s) used in the study. Two factors cause the discrepancies between attained temperature and the target temperature in gleeble experiments: First, thermal momentum during heating, and second quench response time of the machine. It has been noted that these two factors are only significant in short holding time (0.2 s to ~1 s) experiments. In order to resolve these issues in shorter holding times, the set thermal profile was modified slightly in the utilized thermal programs for more accurate attainment of the target temperatures. An example of the discrepancy between the target and achieved temperatures is shown in Figure 2b. Such slight discrepancies in tempering were determined to have a negligible effect in previous studies [33].

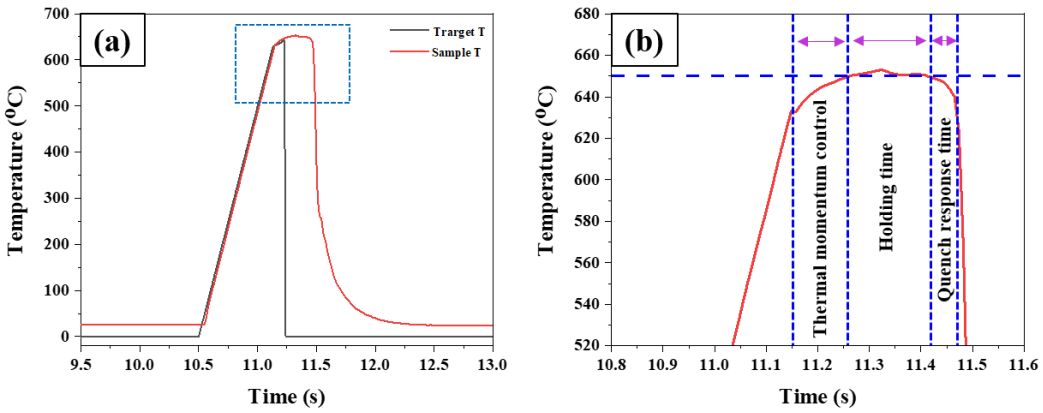


Figure 2: Sample rapid tempering thermal profiles; (a) Rapid tempering thermal cycle for 0.2 s at 650 °C showing the target and sample temperature, (b) detailed illustration of the graph (a) showing the discrepancies in sample temperature.

The investigated tempering time and temperature combinations are shown in *Table 4*. It should be noted that 0.2 and 0.5 s tempering times are only used for tempering temperatures greater than 400 °C. The 0.2 and 0.5 s tempering times have been removed for 350 °C tempering temperature as it is known that no significant microstructural alterations occur at such low tempering time and temperature combination [33]. Moreover, a series of furnace tempering experiments (4, 8, and 24 hrs.) were performed at 650 °C to understand the extent of the tempering phenomenon at such extreme conditions.

Table 4: Temperatures and times used for rapid tempering heat treatments

Temperatures (°C)	Time (s)	
	Gleeble 3500	Furnace
350	1, 2, 5, 10, 20, 60	-
400, 450, 550	0.2, 0.5, 1, 2, 5, 10, 20, 60	-
650	0.2, 0.5, 1, 2, 5, 10, 20, 60	450, 900, 1800, 3600, 14400, 28800, 86400

Microhardness measurements were conducted using a Clemex CMT automated hardness tester interfaced with a Vickers indenter according to ASTM E384 [40]. Hardness line scans at 45° orientation were measured through the thickness direction. 18 indents were made in total on each sample. The indentation

pattern has been schematically shown in *Figure 1*c. Indentations were made using a 200-gram force and 15 s dwell time. All the microhardness data presented are the average of at least 16 measurements. It should be noted that the two indents closest to the sheet surfaces were ignored in all average microhardness measurements to eliminate the influence of artifacts on microhardness measurements. All error bars represent the 95% confidence interval (CI) value. High-density microhardness maps of 3G steels were also made to quantify the hardness values of all major regions within the typical RSW. A 100-gram force with a 15 s dwell time was used in this case. The distance between the indents was 100 μm, which is greater than three times the diameter of each indentation.

The metallographic analysis was done using the scanning electron microscope JEOL JSM 7000F. The samples were ground and polished to 1 μm diamond finish level using standard metallographic techniques. After sample preparation, 2% Nital solution was used for etching the metallography samples for 10 seconds to reveal the microstructure.

Standard transmission electron microscopy (TEM) thin foil samples were prepared to examine the microstructure of the samples heat-treated with 650 °C-60 s, and 450 °C-0.5 s. The samples were ground to approximately 80 μm thickness using the standard metallographic techniques. Afterward, 3 mm diameter discs were punched out of these samples. These discs were thinned using Struers TenuPol-5 twin jet electrolytic polishing in a solution of 10% perchloric acid and 90% methanol maintained at -40 °C, at a voltage of 20.5 V. Carbon extraction replicas were prepared by depositing a thin carbon film on the surface of the etched (2 % nital solution) samples. After sectioning the carbon film into small pieces by scribing, the sample was immersed in a solution of 5 % nital to float the carbon film with particles. A copper grid was used to collect those pieces and dry them before observing them under the TEM. All the TEM samples were analyzed under a Talos 200 TEM at an accelerating voltage of 200 keV. EDX analysis and selected area diffraction pattern (SADP) analysis were used to identify the carbides present in the materials.

An extensive particle size analysis was conducted on the transmission electron micrographs from the carbon extraction replica. The procedure employed in this study was the same as that used by Biro *et al*. [33]. The micrographs were analyzed with ImageJ software. Regardless of their shape, all the particles were analyzed, regardless of size. Particle areas were individually measured. The particle diameters were calculated as per their circular diameter (the diameter of a circle having the same area as the measured particle).

Results

The micrographs corresponding to the microstructures of both BM and SCHAZ of all three investigated spot welds have been shown in

Figure 3. It can be seen that the BM microstructure of both 3G steels consists of a combination of a ferritic matrix with embedded martensite, bainite, tempered martensite, and retained austenite, whereas the microstructure of PHS 1500 BM is fully martensitic. The microstructures were confirmed from their corresponding morphologies [41,42]. It should be noted that the volume fraction of martensite and bainite in 3G 1180 is higher than the 3G 980 but, the fraction of TM is higher in the 3G 980 BM than the 3G 1180 BM. The 3G 1180 had a higher martensite volume fraction than the 3G 980, which is in good agreement with the reported higher mechanical properties of 3G 1180 steel, as shown in *Table 2*.

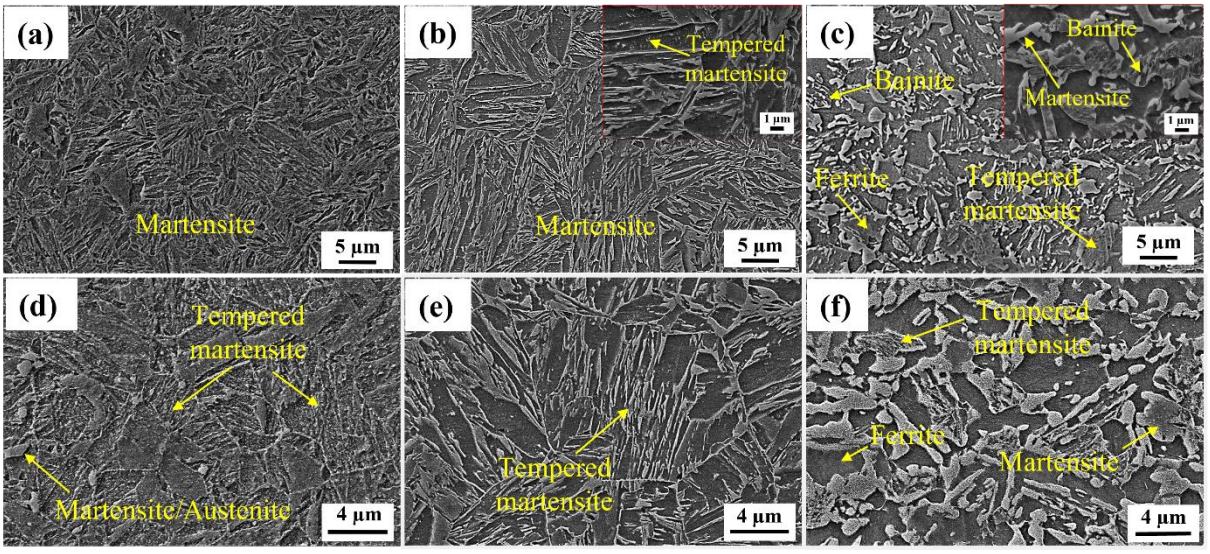


Figure 3: Scanning electron micrographs of the investigated spot welds; (a) PHS 1500 BM, (b) 3G 1180 BM, (c) 3G 980 BM, (d) PHS 1500 SCHAZ, (e) 3G 1180 SCHAZ, and (f) 3G 980 SCHAZ

The SCHAZ of PHS 1500, on the other hand, consists of a large volume fraction of TM (see *Figure 3*d) which has a lath morphology. The lath martensite present in the 3G 1180 transformed into tempered martensite, but the blocky martensite present in the 3G 980 transformed into small pockets of TM as shown in *Figure 3e-f*, respectively. It has been noted that the microstructure of the SCHAZ is similar to that of BM since the temperature exerted in SCHAZ is less than the austenite transformation temperature (A_{c3}).

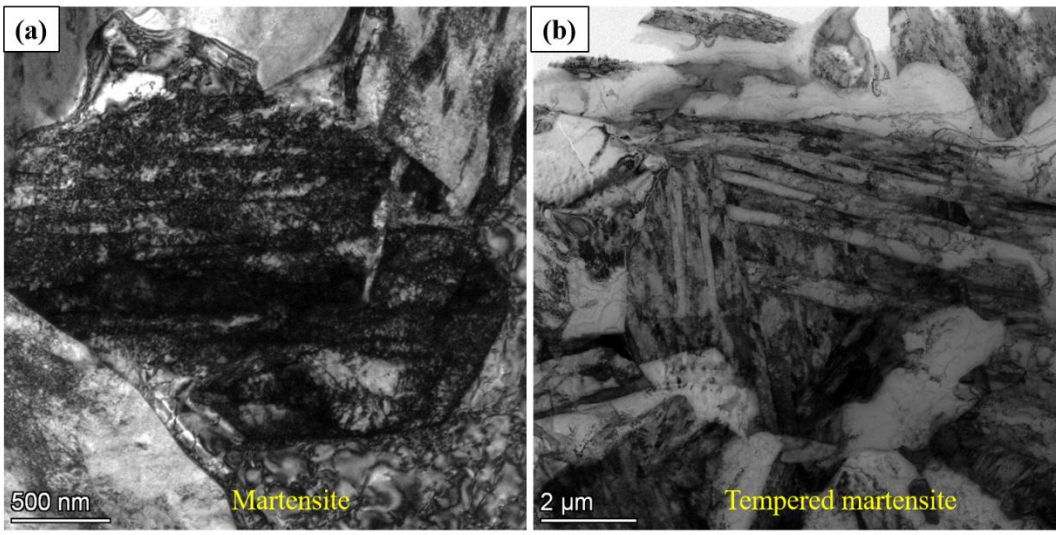


Figure 4: Bright field images of (a) martensite, and (b) TM present in the 3G 980 steel base material

The TEM micrographs of the martensite and TM in the as-received 3G 980 steel are shown in *Figure 4*. The cementite particles are present at the lath boundaries of the TM (see *Figure 4*b). Furthermore, evenly distributed fine carbides were present throughout the matrix of 3G 980, and 1180 steels as shown in *Figure 5*. *Figure 5*a shows a bright-field image of the carbides present in the as-received 3G 980 steel. Cuboidal and spherical-shaped carbides (see *Figure 5*b and d) are present in the steels and their corresponding diffraction patterns are illustrated in *Figure 5*c and e, respectively. The observed cuboidal particle had an

FCC crystal structure and also showed an orientation relationship with the surrounding ferrite ($[001]_{Carbide} \parallel [\bar{1}23]_{\alpha}$). This cuboidal-shaped particle is confirmed as TiC from the diffraction pattern and X-ray spectroscopy (EDX) analysis. The size of the cuboidal-shaped carbides was about 20 nm, whereas the spherical particles were about 25 nm, in 3G 980 steel. The presence of these types of carbides was also reported in recent literature [43,44]. Furthermore, spherical-shaped particles were primarily observed in the as-received 3G 1180 steel as shown in *Figure 5*f, with an average size of 30 nm. A typical spherical-shaped particle and its corresponding diffraction pattern are shown in *Figure 5*f and g. It can be seen that the particle had a BCC crystal structure, as seen in *Figure 5*e. For instance, the spherical carbide in *Figure 5*d was Ti-rich with slight Mn and Si. Saha *et al.* [28,29] reported similar types of carbides in as-received dual phase 780 steels, and proposed that slight changes in chemical composition can be observed in carbides according to the composition of the base materials.

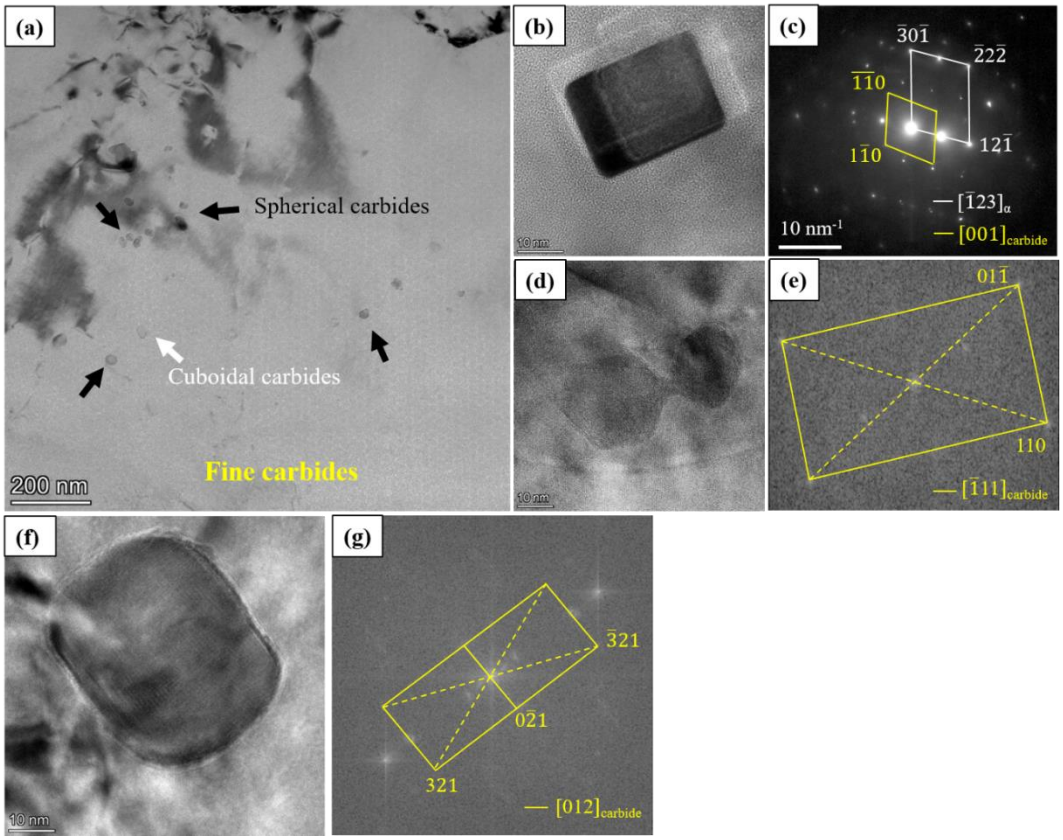


Figure 5: Microstructures of the carbides from as-received 3G 980 and 3G 1180 steels. (a) Distribution of fine carbides in the as-received 3G 980 steel, (b and d) cuboidal shapes and spherical carbides, and (c and e) their corresponding diffraction patterns. (f and g) spherical particles present in the 3G 1180 steel and its diffraction pattern, respectively.

Figure 6 illustrates the microhardness profiles from the base material to the center of the FZ of the welds according to the AWS standard. The different areas of the investigated welds are marked as BM, HAZ, and FZ in the graph. The average BM and FZ hardness are 491±1 HV and 487±4 HV for PHS 1500; 397±3 HV and 477±9 HV for 3G 1180; and 295±4 HV and 510±8 HV for 3G 980, respectively. While both the PHS 1500 and 3G 1180 show softening in the SCHAZ, the 3G 980 SCHAZ showed an increase in the hardness by 22 HV compared to the BM hardness. This increase in the hardness of SCHAZ for 3G 980 welds is suspected to be due to secondary hardening and is consistent with the reported literature by Shamsujjoha *et al.* [45], Figueredo *et al.* [3], and Ramachandran *et al.* [46] on spot-welded 3G steels. The secondary

hardening was also reported in fiber laser welded DP 780 [28] DP 980 [29] steels. It has been reported that secondary hardening is a material characteristic, and its occurrence does not depend on the joining process (temperature histories) [28]. High-density hardness maps across the welds in 3G 980 and 3G 1180 were shown in *Figure 6*b and c, respectively. The hardness profiles (line scans) extracted from corresponding maps are also shown in *Figure 6*d and e. As illustrated the extracted hardness profile from high-density hardness maps shows inline with the profile shown in *Figure 6*a. The secondary hardening and softening that occurred in welds can be clearly seen from the extracted profile, in 3G 980 and 3G 1180 respectively. Thus the authors confirm that a clear secondary hardening happens in 3G 980 and only softening happens in 3G 1180 respectively, during resistance spot welding.

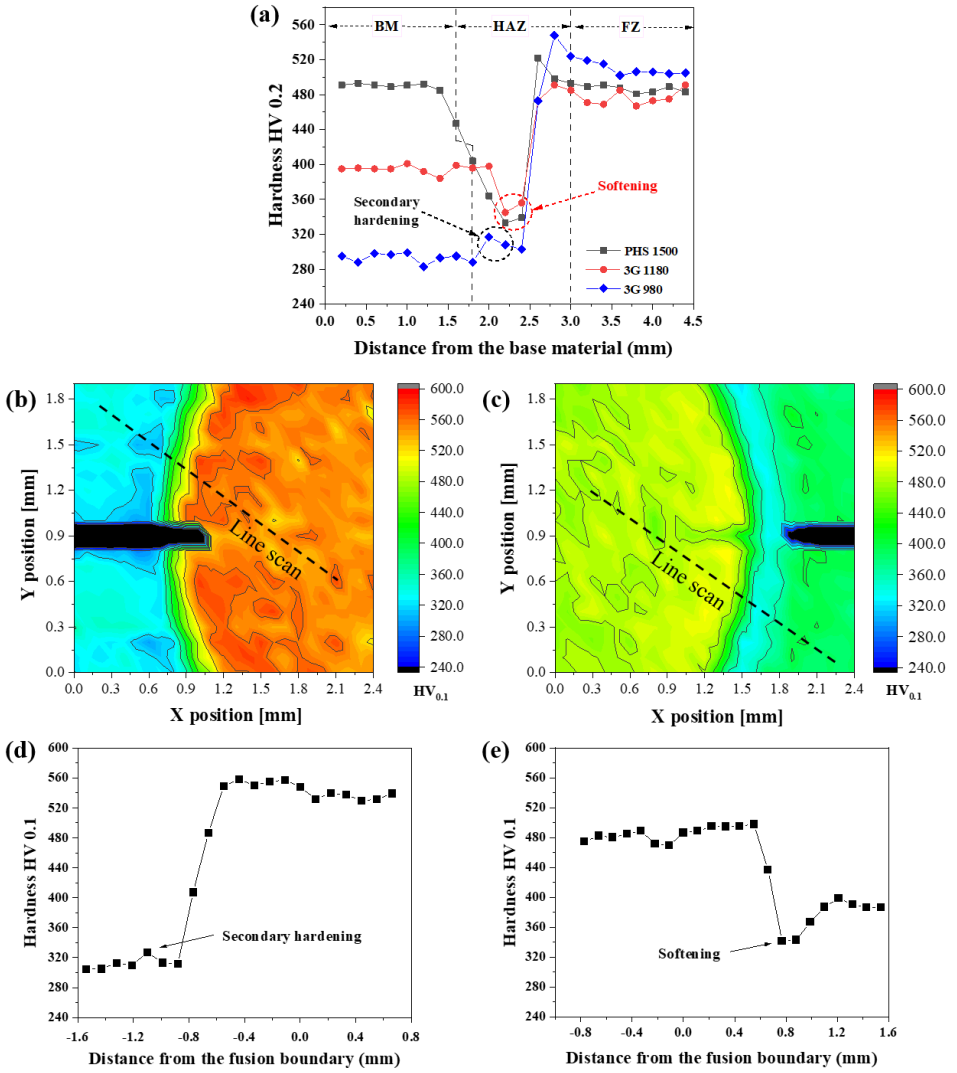


Figure 6: Microhardness profiles across the welds of PHS 1500, 3G 1180, and 3G 980 steel spot welds. High-density hardness maps and line scans extracted from corresponding graphs (b and d) 3G 980, and (c and e) 3G 1180 show the secondary hardening and softening, respectively

Isothermal tempering experiments, performed in a Gleeble 3500 thermo-mechanical simulator reproduced the SCHAZ microstructure of the weldments. Biro *et al.* [47] pointed out that the extent of tempering (tempering progression) increases with an increase in tempering temperature. At relatively higher temperatures atomic diffusion will speed up, increasing the rate of diffusion-driven metallurgical transformations, thereby it increases the rate of tempering. Therefore, longer tempering times such as

86,400s (24 hrs.) experiments were carried out at 650 °C in a furnace, to identify the maximum possible tempering progression where softening no longer continues to advance appreciably. The rationale behind performing the long holding times, i.e. 450 s (7.5 min.) to 86,400 s (24 hrs.) for 650 °C, experiments within a furnace was to avoid complexities associated with using a gleeble simulator at such extended times.

The average hardness of all heat-treated samples is plotted in *Figure 7*. It is noted that PHS 1500 shows softening in all the selected tempering conditions (see *Figure 7a*), which agrees with the results from the literature [15,33,47–49]. In 3G 1180 steel, noticeable tempering happens with tempering temperatures of 550 °C onwards, as shown in *Figure 7b*. Despite the tempering time, lower tempering temperatures up to 450 °C, lead to no significant difference in hardness (~ 4 HV difference in each temperature). As the temperature increased, between 350 and 400 °C, the hardness dropped slightly (~ 7 HV), and was constant throughout the tempering time. However, it is interesting to note that at 450 °C, an increase in hardness was measured; this is especially noticeable at lower tempering times of 0.2 and 0.5 s. Although hardening was observed, these hardness values are still lower than the BM hardness (397±3 HV). At 550 °C, the hardness negligibly increased (~5 HV) up to 0.5 s tempering time then suddenly decreased to an average of 347±2.7 HV at 20 s tempering time. It can be observed that when the 3G 1180 was tempered at 650°C, the hardness decreased 72 HV below the BM hardness, and did not decrease further until the sample was tempered for more than 60 s. The hardness decreased drastically to 243±3.8 HV at 86,400 s (24 hrs.), but it should be noted that tempering was almost complete after 28,800 s (8 hrs.) since no noticeable changes in hardness were observed thereafter.

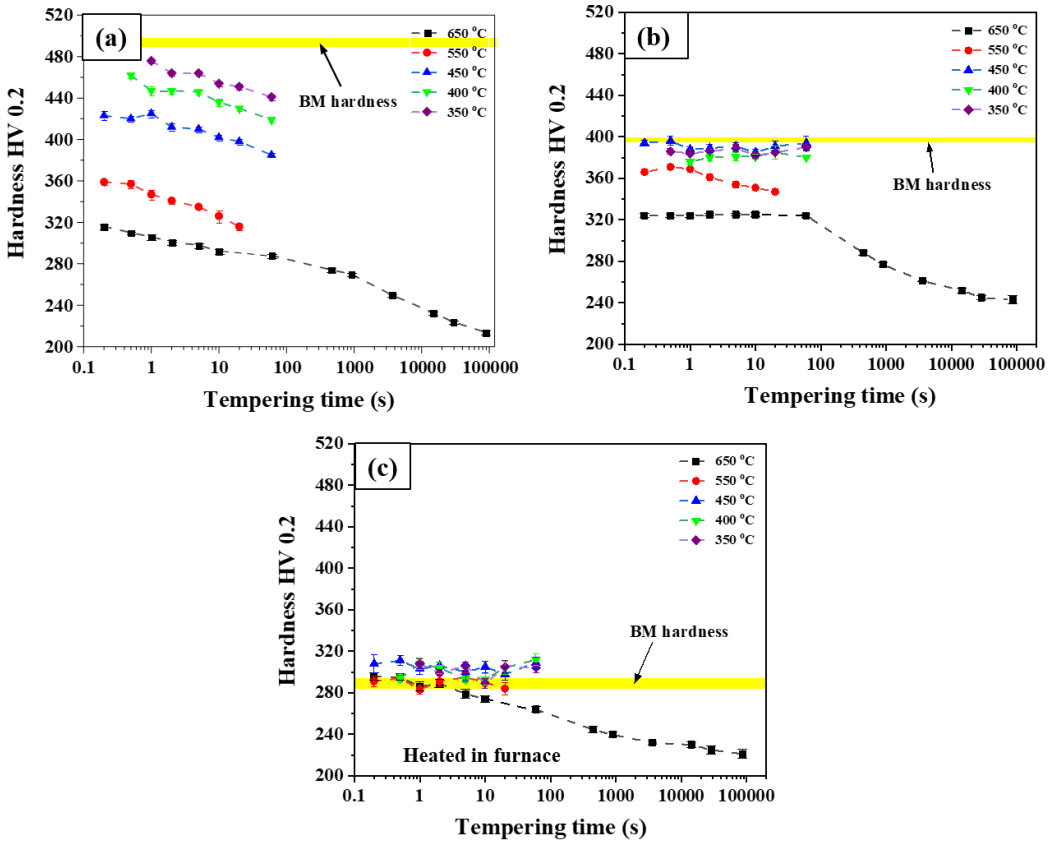


Figure 7: Hardness profiles of the tempered samples (a) PHS 1500, (b) 3G 1180, and (c) 3G 980

In 3G 980, all the combinations of tempering temperatures up to 550 °C show increased hardness compared to that of the BM. At tempering severities beyond 650 °C and 5 s, the hardness values decrease below the hardness of the BM as shown in *Figure 7c*. The highest hardness value measured was from the sample tempered at 450 °C and 0.5 s, where the increase in hardness was 17 HV higher than the BM. This observation is in good agreement with the maximum hardness value measured in the spot weld SCHAZ; 22 HV higher than the BM hardness (see *Figure 6*). The observed changes in hardness with an increase of hold time at 550 °C imply that there exists a competition between secondary hardening and softening in the SCHAZ regardless of the tempering time. Similar behaviors were observed at tempering temperatures and time: 350 °C 10 s and 400 °C 0.5, 5, and 10 s. At 650 °C, a combination of softening and secondary hardening was observed throughout the experimented combination of tempering time and temperature. The

dominant effect up to a tempering time of 2 s was hardening which changed to softening at a holding time of 5 s onwards. The tempering phenomenon in 3G 980 continues to progress at 650 °C up to 3,600 s, then slows down at a longer tempering time, which could be due to the consumption of the available martensite in the original microstructure.

The hardness of the isothermally tempered samples compared to spot weld SCHAZ hardness can be used to determine the tempering kinetics that occurs in the SCHAZ during spot welding. Interpretation of *Figure 7* alongside *Figure 6* shows that 550 °C with 5 s hold time shows similar hardness in the SCHAZ of the PHS 1500 and 3G 1180 welds. However, 3G 980, on the other hand, shows 450 °C for 0.5 s shows good agreement with the hardening observed in the HAZ of the spot welds.

Discussions

The measured hardness values can be used to model the HAZ tempering of steels. The Johnson–Mehl–Avrami–Kolmogorov (JMAK) equation was used previously by different researchers to model the tempering phenomenon in a variety of steel grades [15,33,47]. It is known that the JMAK equation is most accurate in predicting the kinetics of steels that exhibit softening phenomenon. Hence, the validity of such models for 3G 1180 and 3G 980 should be evaluated, as the JMAK equation assumes a constant decrease in HAZ hardness. Although, Holloman-Jaffe's (H-J) model, used as an alternative approach to predict the hardness of the SCHAZ [28,47], can effectively visualize secondary hardening.

The tempering process was related to the tempering temperature and time, the tempering cycle can be generalized using the H-J tempering parameter [50]. The H-J parameter can be calculated using Equations 3 and 4.

$$\text{H-J parameter} = [T(C + \log t)] \qquad \text{Equation 3}$$

$$C = 17.7 - 5.8 \times (\%\ \text{of C}); \text{ for time in seconds} \qquad \text{Equation 4}$$

Where T is the temperature in K, C is a material constant that is related to the C content in the steel, and t is the tempering time in seconds.

The calculated H-J tempering parameters of the Gleeble heat-treated samples are plotted against their corresponding microhardness values in *Figure 8*. It can be seen from *Figure 8a*, that the hardness of the PHS 1500 decreased steadily with increasing H-J parameters regardless of the tempering temperature and time. All the tempered hardnesses are lower than the BM hardness, which implies that only softening phenomenon was active in the PHS 1500 steel. The tempering mechanism on martensitic steels has been the focus of numerous studies [33,48].

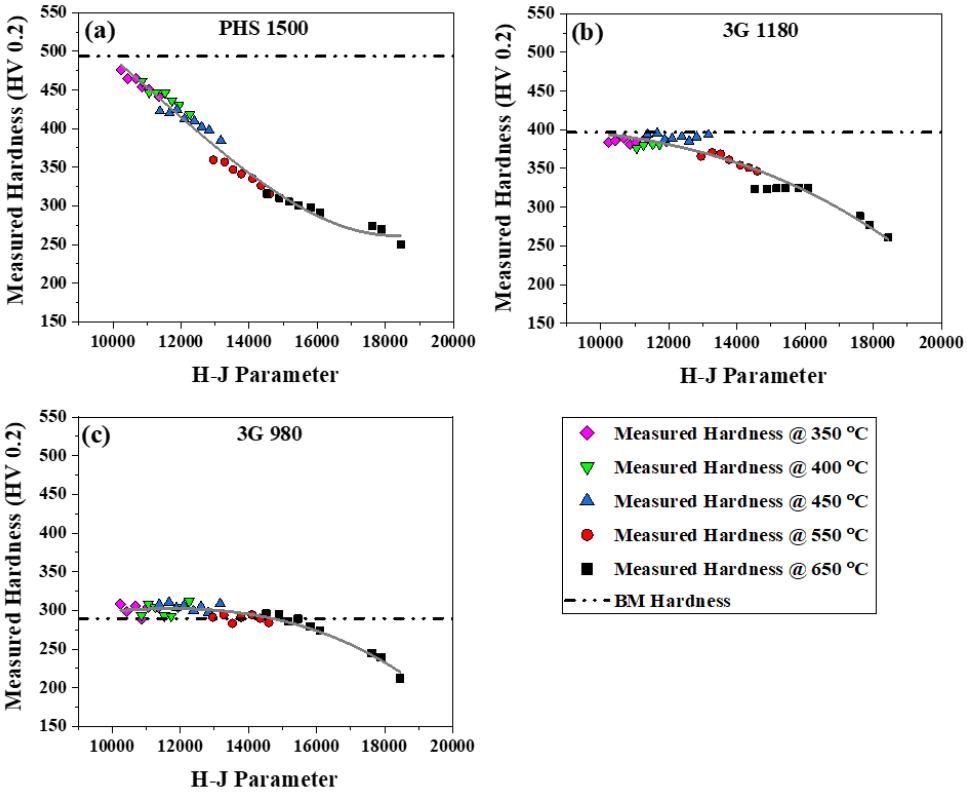


Figure 8: Vickers microhardness as a function of Hollomon–Jaffe tempering parameter of Gleeble rapid tempered and furnace tempered samples for (a) PHS 1500, (b) 3G 1180, and (c) 3G 980

In martensite containing steels, tempering of martensite (carbide nucleation and growth) is the predominant mechanism for softening. Biro *et al.* [33,47,48] associated martensitic tempering with carbide precipitation and growth. The carbide nucleation starts at relatively low temperatures and short tempering times, and thereafter, followed by growth [13,26,51]. Furthermore, Saha *et al*. [28] investigated the tempering response in DP 780 steel and concluded that coarsening of cementite particles in the martensite-containing steel was the key phenomenon happening during tempering, which can increase the effective free length of dislocations and decrease the flow stresses. The hardness data shown in *Figure 7a* shows good agreement with the aforementioned results [33,52]. The results revealed that the tempering in PHS 1500 is a continuous metallurgical phenomenon since severe softening occurred even at the highest tempering times, which is mainly associated with the carbide coarsening effect.

In 3G 1180, the hardness decreases with an increase in the H-J parameter as shown in *Figure 8b*. It should be noted that the hardness remained virtually constant for the low H-J parameter (up to 450 °C) then the slope of the predicted hardness line increases to a maximum. The extent of tempering is almost constant for 650 °C up to 10 s tempering time. 3G 980, on the other hand, showed a combination of softening and secondary hardening behavior as shown in *Figure 8c*. Secondary hardening was observed at all tempering times up to 450 °C. Tempering temperature at 650 °C was the transition zone between secondary hardening to softening. The maximum hardening was measured at a tempering temperature of 450 °C with a 0.5 s tempering duration, which can be also seen in *Figure 7*c.

The microstructural analysis of heat-treated specimens with the maximum hardness (secondary hardening) and the minimum hardness (softening) is important since it assists with understanding the mechanism behind the tempering of 3G steels. It should be noted that the minimum hardness samples were chosen only from the gleeble isothermal tempering experiment, and not the samples heat-treated in the furnace. Therefore, 0.5 second tempering time at a temperature of 450 °C and 60 second tempering time at a temperature of 650 °C was chosen as the secondary hardening and softening samples, respectively. It should

be noted that the H-J parameters of 3G 1180 and 3G 980 steels for the softening conditions are 17,056, and 16,814, respectively. The selected tempering conditions for further analysis are summarized in *Table 5*.

Table 5: The samples chosen for the microstructure analysis and their corresponding H-J parameters

	BM hardness (HV 0.2)	Hardness of 450 °C for 0.5 s (HV 0.2)	Hardness of 650 °C for 60 s (HV 0.2)
3G 1180	396 ± 3	396 ± 4.3 (11659)	324 ± 1.5 (16085)
3G 980	295 ± 4	311 ± 4.6 (11668)	264 ± 2.5 (16096)

Figure 9 shows the electron micrographs of the 3G 1180, and 3G 980 steel isothermally tempered at 450 °C for 0.5 s. The matrix microstructure is almost the same as that of the BM microstructures. 3G 1180 steel sample (396 ± 4) had a hardness closer to the BM hardness (397±3). This also implies that no significant tempering happened at 450 °C for 0.5 s in 3G 1180 steel. However, the tempering progression was not a linear function with tempering time at 450 °C. It was seen that hardness slightly (~3 HV) increased at lower tempering times and then decreases at higher tempering times. This slight increase in hardness is insignificant when accounting the 95% confidence interval. Microstructure in *Figure 9a and b* show that the lath martensite/bainite present in the BM starts transforming into ferrite and carbides by carbon partitioning. However, small patches of untransformed martensite can also be seen in *Figure 9b*. Furthermore, isothermal tempering at 450 °C for 0.5 s resulted in the fine decoration of sub-micrometer particles (carbides) along the prior austenite, block, and lath boundaries. The carbides present were finer (average size of 55 nm for cuboidal-shaped and 52 nm for spherical-shaped) than in the softened conditions. 3G 1180 steel had rich chemistry compared to 3G 980 steel. The carbon equivalent of 3G 1180 is 0.70 compared to 0.64 for 3G 980.

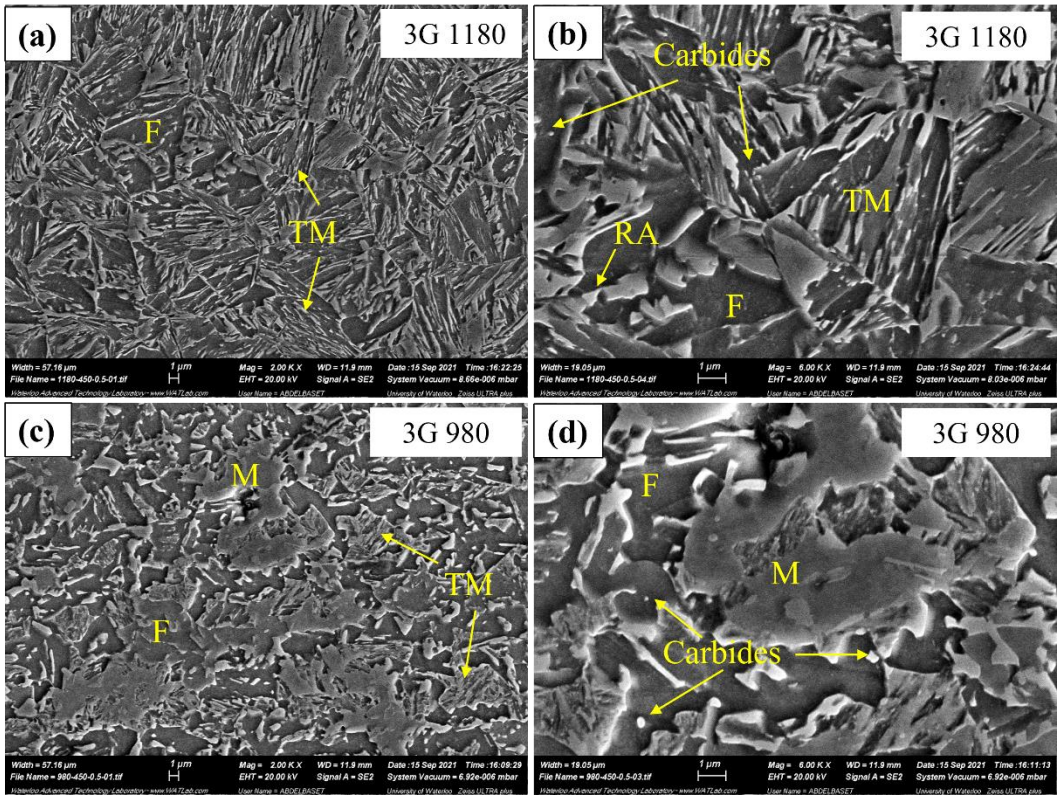


Figure 9: Electron micrographs of samples tempered at 450 °C for 0.5 s; (a and b) 3G 1180 steel with a hardness closer to BM hardness, and (c and d) secondary hardened 3G 980

3G 980 steel (450 °C for 0.5 s), shows a significant increase in hardness, which is considered to be the secondary hardening. It has been reported that the secondary hardening in high-strength steels is mainly related to (1) type, (2) morphology, (3) volume fraction, and (4) distribution of carbides [53,54]. Although a small volume fraction of TM was present in the BM of 3G 980 steel, the fresh martensite present in the BM started decomposing into ferrite and cementite in the secondary hardened sample, as seen in *Figure 9*d. The partial recovery of microstructure happened in these fresh martensite leaves intra and interlath carbides, which pins the movement of dislocations, as shown in *Figure 10*. Furthermore, the carbides present in the samples are fine, with near-spherical (~ 40 nm) and plate-like (~ 35 nm) morphologies. The interaction between the particles and dislocations can be seen in *Figure 10b*. The nucleation of carbides can happen in high-angle grain boundaries (prior austenitic grain boundaries, and block boundaries), low-angle

boundaries (lath boundaries), and, in the lattice defects such as dislocations [22]. Hence, it can be concluded that the small intralath carbides seen in the 3G 980 could be nucleated at the grain boundaries. Furthermore, the dislocations found in the ferrite phase are attributed to insufficient time for complete recovery. This is also consistent with previous literature on tempering on DP steels [22–24].

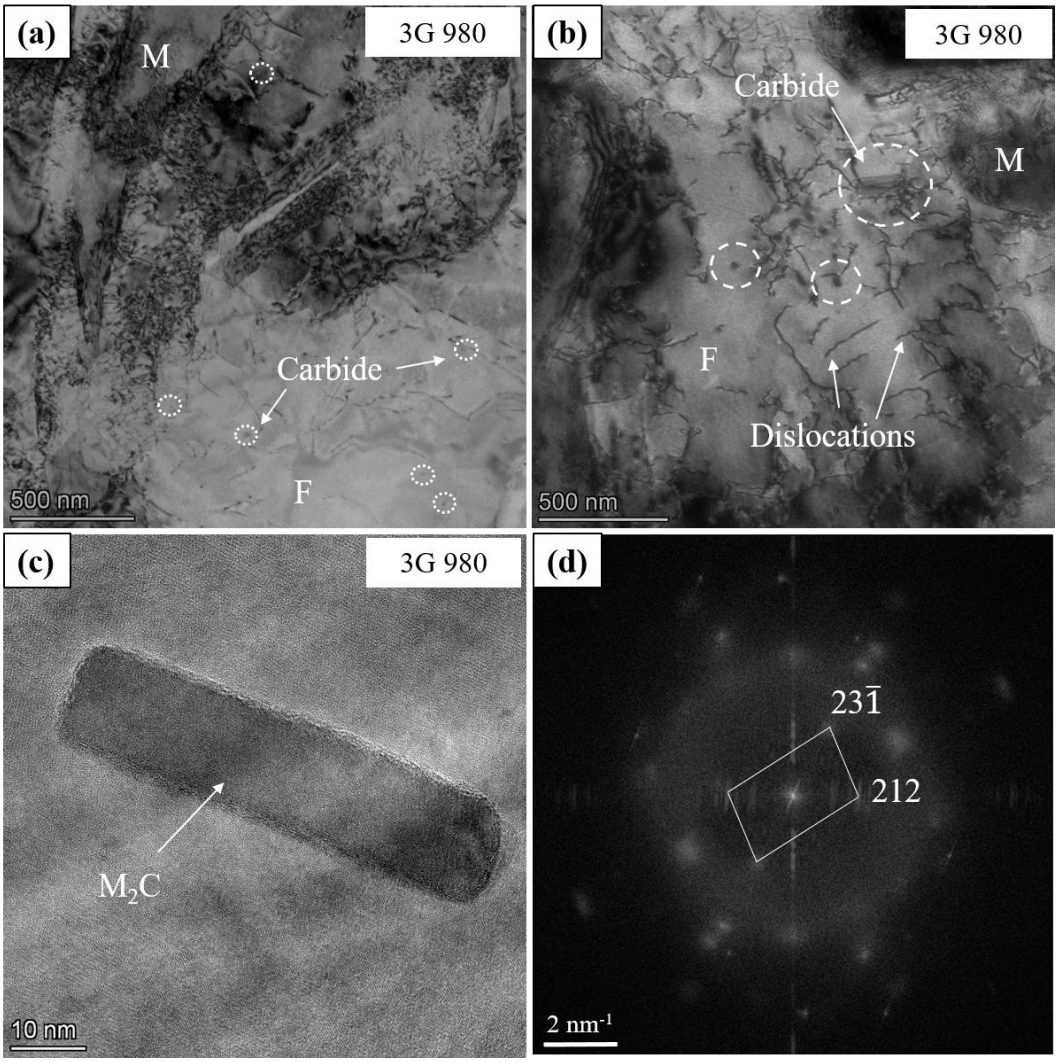


Figure 10: Transmission electron micrographs showing the presence of small carbides in the matrix after tempering at 450°C for 0.5 s in 3G 980 steel (a) microstructure start decomposing with small carbides, and (b) another image showing the interaction between dislocations with plate-shaped carbide, (c) a typical plate-shaped M_2C carbide and its (d) corresponding diffraction pattern

An example of a particle, responsible for secondary hardening behavior observed in the 3G 980 steel which was tempered at 450°C for 0.5 s and its corresponding diffraction pattern are shown in *Figure 10*c, and d, respectively. The particle present in the microstructures can be confirmed by the EDX analysis interfaced with the TEM. The EDX analysis revealed the investigated particles are M_2C typed with a complex crystal structure, where M represents metallic elements such as Ti, Mo, Mn, Si, and Al, as shown in *Figure 11*b. These results agree with the literature where it has been reported that the M in steels can be either of the metallic element or a complex combination of those. For example, Shen *et al.* reported that M is a combination of Ti, Mo, Cr, Nb, Mn, and V in ferritic steels, with a complex cubic structure [55]. Furthermore, the high-resolution TEM lattice image shown in *Figure 10*c indicates that the M_2C typed particle is coherent with the ferrite matrix, which can effectively pin the movement of dislocations as shown in *Figure 10*b.

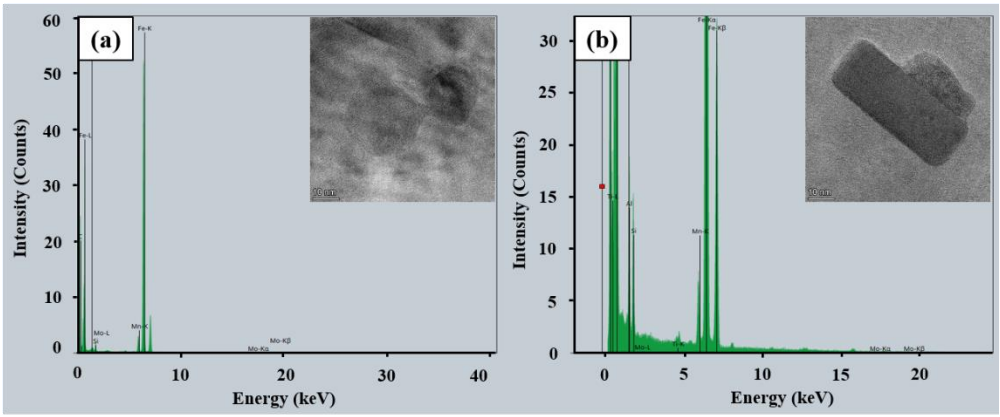


Figure 11: EDX spectrum and its corresponding TEM images of the carbides present in 3G 980 steel, (a) as-received steel, and (b) tempered at 450°C for 0.5 s

TEM bright field image showing the particle-free matrix microstructure of 3G 1180 steel, tempered at 450 °C for 0.5 s is shown in *Figure 12*. As mentioned above (see *Figure 6*) the secondary hardening was not observed in the 3G 1180 steel. *Figure 12* shows, the matrix microstructure in 3G 1180 steels, and it should be noted that the microstructure is free from secondary carbides. Furthermore, the carbides present in the base material are still present even after the tempered condition.

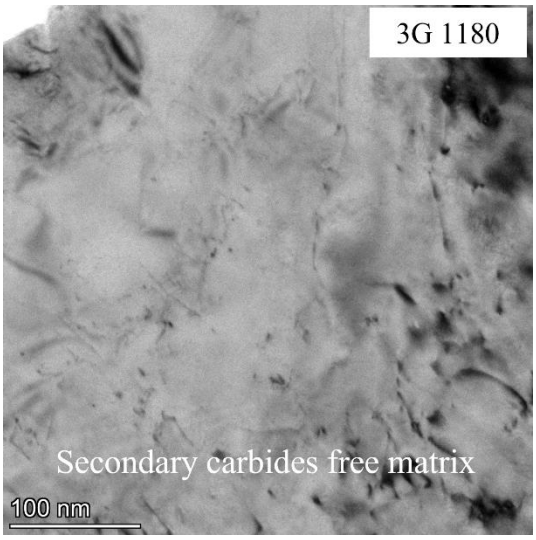


Figure 12: TEM micrograph showing the secondary carbide-free matrix microstructure when tempered at 450 °C for 0.5 s

High-resolution TEM images and their corresponding EDX spectrum of 3G 980 as-received steel and tempered at 450°C for 0.5 s are shown in *Figure 11*a and b, respectively. EDX analysis of a typical carbide present in the as-received steel confirmed the presence of Mo, Mn, and Si along with the parent Fe. The size of the analyzed particle was in the order of 20 nm; hence it is widely accepted that the peaks of matrix Fe will be dominated in the EDX spectrum due to the limitation of aperture size in the experimented microscope. Furthermore, according to Jang *et al.* [56], the presence of other alloying elements such as Mn and Si in these carbides can slightly change the lattice parameters. However, the EDX spectrum of a typical plate-shaped carbide in 3G 980 tempered at 450°C for 0.5 s shows the strong peaks of Ti and Mo along with the Mn, Si, Al, and Fe. Precipitation of different carbides, their composition, and their mechanisms are out of the scope of this work and will be discussed in future works.

The electron micrographs of the softening phenomenon happening in 3G steels are shown in *Figure 13*. The micrographs show that the microstructure of 3G 980 mainly consists of ferrite, martensite (M), TM, and secondary carbides. Carbides are mainly distributed at the grain boundaries, as grain boundaries are the potential sites of carbide nucleation (*Figure 13b and d*). Isothermal tempering in 3G 1180 shows the

presence of large carbides on the grain boundaries and inside the TM grains as shown in *Figure 13b.* At high tempering time (60 s) all martensite present in the BM is transformed into TM both in 3G 1180 and 3G 980.

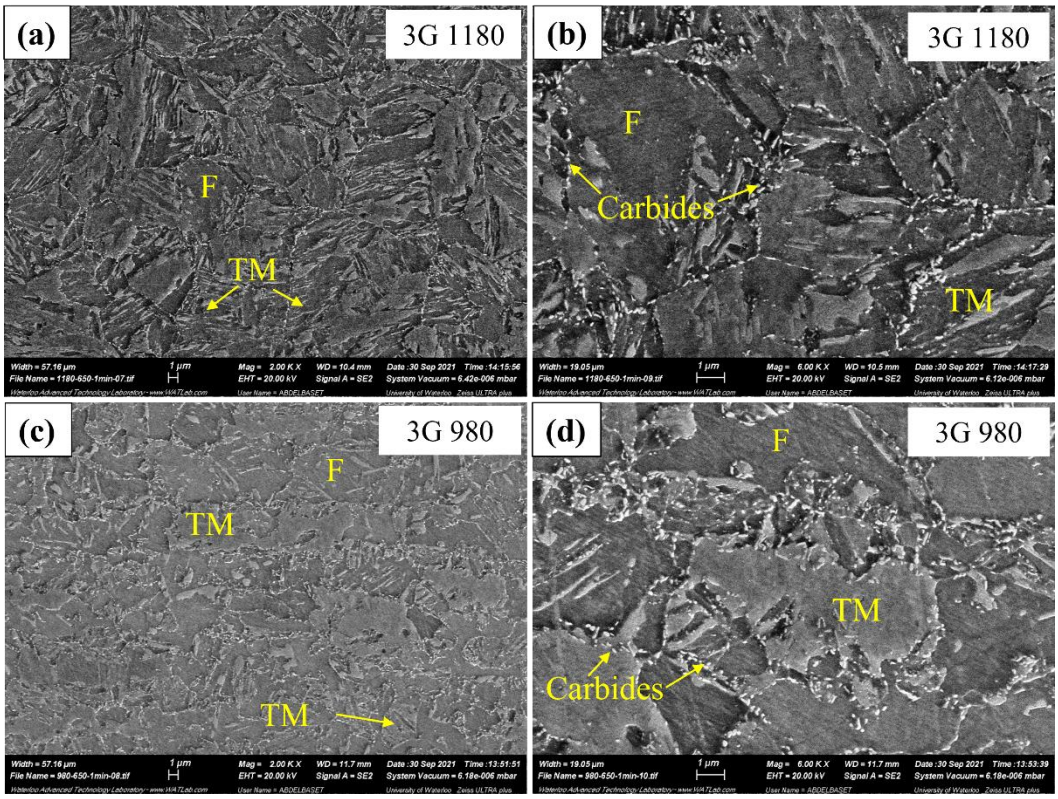


Figure 13: Electron micrograph showing different phases present in the sample showing softening phenomenon (650 °C for 60 s); (a and b) 3G 1180, and (c and d) 3G 980

Transmission electron micrographs of 3G 1180 and 3G 980 are shown in *Figure 14a and d*, respectively. In 3G 1180 steel isothermal tempering at 650 °C for 60 s shows clusters of decomposed martensite (ferrite and spherodized cementite) and ferrite. A small fraction of twinned martensite was also seen in this steel (*Figure 14a*). 3G 980, on the other hand, consists of large blocks of decomposed martensite with ferrite (*Figure 14d*). The decomposed martensite is either transformed from the fresh martensite or TM present in the base material. The needle and spheroidal-shaped secondary carbides found in the material had an average size of 150 nm and 83 nm, respectively in 3G 1180, whereas in the case of 3G 980 they were

123 nm, and 74 nm, respectively. Both kinds of carbides can be seen in *Figure 14a and d*. It can be also seen that the large spheroidal-shaped carbides are mainly concentrated inside the grains. Furthermore, needle-shaped carbides are mainly seen in the martensite lath boundaries (*Figure 14a*). The recovery of martensite can be further confirmed by the extensive reduction in dislocation density and disappearance of prior martensitic lath boundaries (see *Figure 14*), which is also reported in the literature [20]. It was also observed from the TEM micrographs that the ferrite seen in both steels is dislocations free. These observations are in-line with the martensite and carbide morphology reported in the literature [20,47]. According to Baltazar *et al*. [13], the tempering progression of martensite happens in a series of steps, where the martensite decomposes into ferrite and small needle-shaped cementite. This cementite spherodizes on the lath boundaries, which is followed by the coarsening of the cementite leading to the elimination of underlying martensite structures.

The carbides present in the 3G steels have been identified by the selected area diffraction (SAD) pattern analysis, as shown in *Figure 14*c and f. *Figure 14*b shows a typical example of carbide present in the 3G 1180 steel heat treated at 650 °C for 60 s. The SAD pattern extracted from the carbide is shown in *Figure 14*c. SAD pattern indexing depicts that the identified carbide is cementite (Fe_3C) with an orthorhombic crystal structure. The cementite particles were evenly distributed inside the grains. The cementite particle also shows the orientation relationship with the matrix ferrite ($[\bar{5}\bar{4}4]_\theta \parallel [00\bar{4}]_\alpha$).

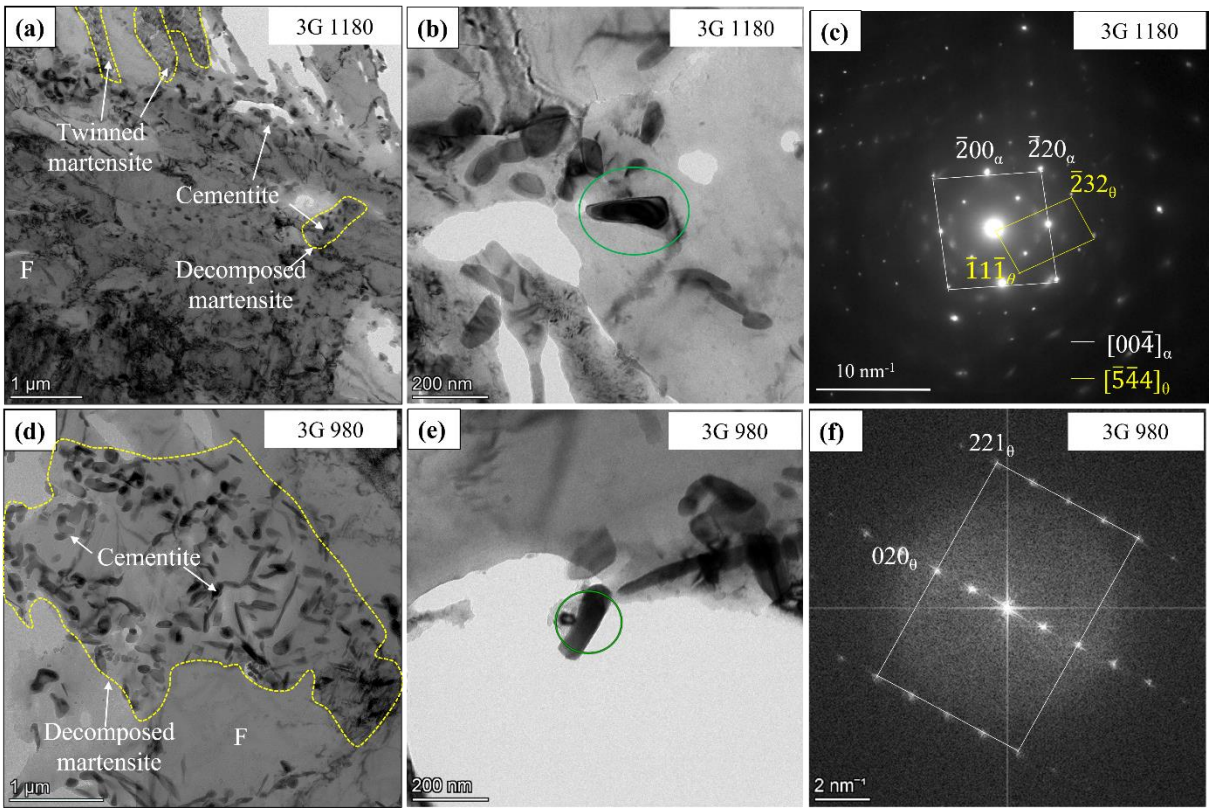


Figure 14: Transmission electron micrographs of samples, typical carbide, and corresponding SAD pattern of the carbides tempered at 650 °C for 60 s. (a to c) 3G 1180, and (d to f) 3G 980.

Once the particles were identified by the TEM analysis, the distribution, and size of the particles were measured by analyzing the carbon extraction replica micrographs. The size and distribution of the particles were measured using Image J software. The detailed distribution and size of the particles in 3G 980 as-received steel, tempered at 450°C for 0.5 s, and tempered at 650°C for 60 s were shown in *Figure 15* a, b, and c, respectively. The geometric average size of the particles present in the as-received steel is 28 ± 5.3 nm, and it shows good agreement with *Figure 5*. It should be noted that the particles include the spherical, and cuboidal-shaped particles and the cementite particles present in the tempered martensite. The number density of the particles continuously decreases after the size of 30 nm. During tempering at 450°C for 0.5s, the M_2C typed carbides with an average size of 35 ± 4.0 nm were formed in the steels, as shown in *Figure 10*b. Saha *et al.* [28,29] reported that secondary hardening in DP 780 steel was due to the transformation of

pre-existed carbides in the as-received steel into fine M_4C_3 and M_2C carbides during short tempering. The tempering of 3G 980 steel in this study also agrees with the literature. The number density of the fine particles present in the as-received steel (see *Figure 5*) decreases during tempering at 450°C for 0.5 s. These particles dissolve at high temperatures and act as a carbon source to form M_2C typed carbides during tempering.

Furthermore, the long tempering time such as 550°C for 60 s, the martensite present in the steel microstructure transforms into TM and the final microstructure mainly contains TM with coarse cementite particles (see *Figure 13*). As seen in *Figure 15*c, the particles present in the steel are coarser, which is approximately a size of 100 nm (see *Figure 14*). It should be noted that there were not many fine particles retained in the microstructure after the 550°C for 60 s tempering. Chen et al. [57] reported that carbon migration to retained austenite from martensite in 3G steel is also possible during the experimented temperatures and short time like 1 s, which can stabilize the retained austenite even further. Moreover, according to the carbon content in the steel, the formation of martensite can be changed into twinned martensite under carbon migration. These concepts are not discussed in this paper; however, they will be investigated in future works.

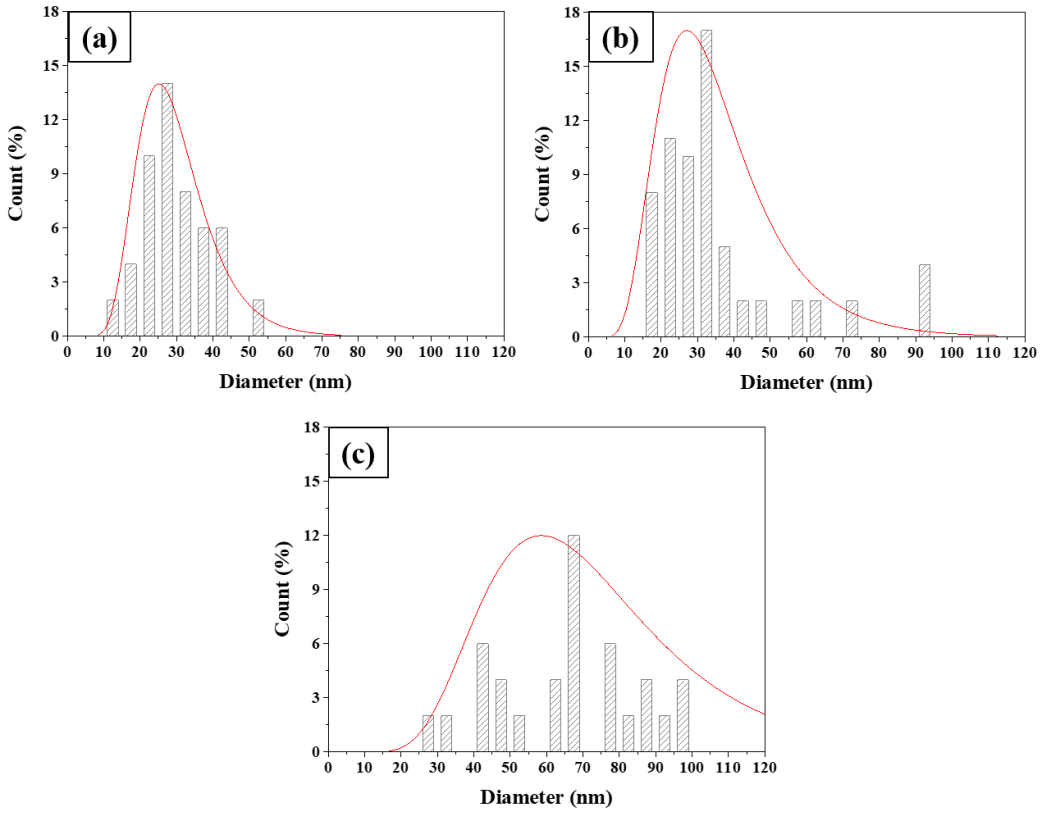


Figure 15: Particle size and distribution in 3G 980 steel. (a) as-received steel, (b) sample tempered at 450°C for 0.5 s, and (c) sample tempered at 650°C for 60 s

Schematic representations of the microstructure transformations during the tempering heat treatments are shown in *Figure 16*. The as-received steel contains martensite, tempered martensite, and particles (see *Figure 5*), as shown in *Figure 16*a. When the as-received steel is tempered at 450°C for 0.5 s, the carbides present in the steel dissolve and produce more carbon in the matrix, and this carbon is combined with elements such as Ti, Mo, Mn, Si, and Al, to form needle-shaped M_2C carbides (see *Figure 10*c and *Figure 11*b). Moreover, these M_2C carbides interact with the dislocations and improve the hardness of the material (see *Figure 16*b). When subjected to a tempering heat treatment of 650°C for 60 s, as tempering is a continuous process, the microstructure will quickly produce the structures and products seen in *Figure 16*b. Before the termination of the heat treatment, the M_2C carbides formed at the start of the heat treatment will

dissolve, which will be replaced by cementite that rapidly coarsens, as shown in *Figure 16*c, leading to significant softening in the steel.

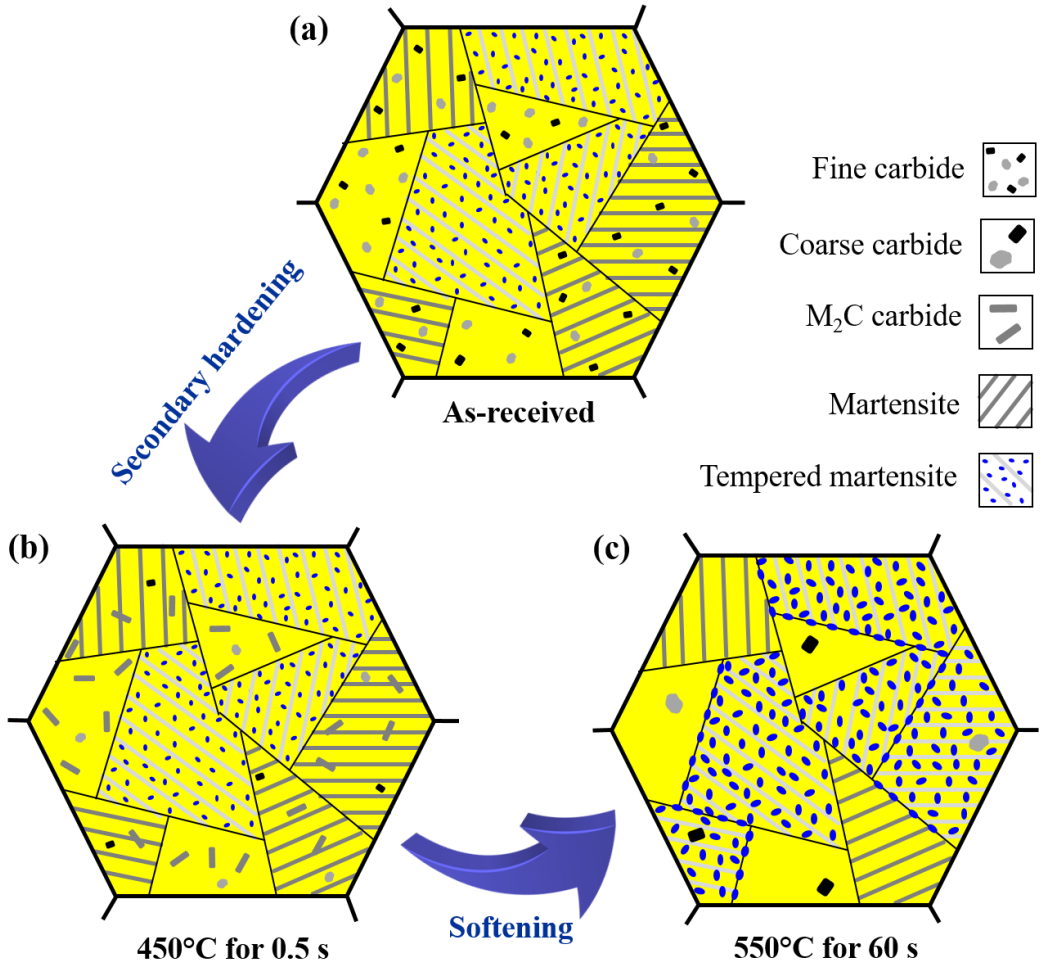


Figure 16: Schematic representation of the microstructural transformations during tempering of 3G 980 steel (a) as-received steel, (b) sample tempered at 450°C for 0.5 s, and (c) sample tempered at 650°C for 60 s

The tempering phenomenon in 3G 1180 and 3G 980 steels was systematically analyzed by an isothermal tempering technique. 3G 1180 shows only softening whereas 3G 980 shows a combination of softening and hardening as discussed above. Carbide precipitation and its growth followed by the recovery of TM is the reason for softening in both the steels. On the other hand, fine plate-like carbide precipitation and pinning

of dislocation movement by those carbides are the reasons for secondary hardening in 3G 980 steel. The hardness values obtained from isothermal tempering results agree with the hardness values of non-isothermally tempered samples (RSW) as shown in *Figure 6*. Hence, the isothermal tempering data can be used to explain the SCHAZ tempering phenomenon that happened in 3G 1180 and 980 steels. Our future effort will focus on the effect of steel chemistry and the orientation relationship of the carbides with the matrix microstructures.

Conclusions

Tempering phenomena during the RSW of 3G 1180 and Ge 3 980 steels were systematically examined by performing isothermal tempering experiments using Gleeble thermo-mechanical simulations. The PHS 1500 included in this study acts as a baseline material since the mechanism of PHS 1500 tempering was already known in the scientific community. Hardness analysis followed by the microstructure analysis was conducted to examine the tempering progression happening in the 3G steels and compared it to the hardness and microstructure of real RSW welds. The following conclusions can be drawn from this study:

1. Tempering progression can be successfully modeled using the H-J parameter. All the models are subjected to the specific material and chemistry. PHS 1500 steel shows complete softening during tempering even at low temperatures and time, whereas 3G steels took some more time and temperatures to show softening.
2. Secondary hardening in 3G 980 steel identified in this study during isothermal tempering happened for a comparatively smaller H-J parameter. The hardness profiles after isothermal tempering agreed well with the hardening peak observed in the experimented resistance spot welded sample.
3. 3G 1180 steels show only softening during the isothermal tempering process. The maximum softening happens with the tempering temperature of 650°C for 60 s. The decomposition of the martensite into ferrite and coarse carbides is attributed to the reason behind softening. Hardness across the weld nugget of 3G 1180 steel also agrees with the isothermal tempering studies. Secondary hardening is not

prominent in the 3G 1180. The TEM observation at 450°C for 0.5 s shows the secondary carbides-free matrix microstructure, which provides evidence of no secondary hardening.

4. 3G 980 steel shows a combination of softening and secondary hardening phenomena. Tempering at 450°C for 0.5 s shows the maximum increase in the hardness of 17 HV higher than the base metal hardness (secondary hardening), whereas 650°C for 60 s shows maximum softening during the isothermal tempering. Such hardening behavior of 3G 980 steel is due to the transformation of pre-existing carbides precipitation to fine plate-like M_2C carbides leading to the pinning of the dislocation's movement. Furthermore, during long tempering condition such as 650°C for 60 s the M_2C particles dissolves into the matrix and was replaced by cementite particles.

Acknowledgment

The authors would like to acknowledge the financial support from the Auto/Steel Partnership, the Natural Sciences and Engineering Research Council (NSERC). The electron microscopy was performed at the Canadian Centre for Electron Microscopy (also supported by NSERC and other government agencies).

Declaration of Competing Interest

The authors declare that they have no known competing financial interests or personal relationships that could have appeared to influence the work reported in this paper.

Credit authorship contribution statement

Dileep Chandran Ramachandran: Conceptualization, Methodology, Investigation, Visualization, Writing - original draft. **Abdelbaset R.H. Midawi**: Writing - review & editing, Data curation. **Mohammed Shojaee:** Writing - review & editing, Resources. **Oleksii Sherepenko:** Writing - review & editing, Resources. **H. Ghassemi-Armaki**: Writing - review & editing, Resources. **Elliot Biro:** Supervision, Validation, Writing - review & editing, Resources.

References

[1] M. Shojaee, A.R.H. Midawi, B. Barber, H. Ghassemi-Armaki, M. Worswick, E. Biro, Mechanical properties and failure behavior of resistance spot welded third-generation advanced high strength steels, J. Manuf. Process. 65 (2021) 364–372. https://doi.org/10.1016/J.JMAPRO.2021.03.047.

[2] J.W. Kim, S.P. Murugan, J.H. Yoo, R. Ashiri, Y. Do Park, Enhancing nugget size and weldable current range of ultra-high-strength steel using multi-pulse resistance spot welding, Sci. Technol. Weld. Join. 25 (2020) 235–242. https://doi.org/10.1080/13621718.2019.1680483.

[3] B. Figueredo, D.C. Ramachandran, A. Macwan, E. Biro, Failure behavior and mechanical properties in the resistance spot welding of quenched and partitioned (Q&P) steels, Weld. World. 65 (2021) 2359–2369. https://doi.org/10.1007/s40194-021-01179-z.

[4] S.P. Murugan, J. Kim, J. Kim, Y. Wan, C. Lee, J.B. Jeon, Y.-D. Park, Role of liquid Zn and α-Fe(Zn) on liquid metal embrittlement of medium Mn steel: An ex-situ microstructural analysis of galvannealed coating during high temperature tensile test, Surf. Coatings Technol. 398 (2020) 126069. https://doi.org/10.1016/j.surfcoat.2020.126069.

[5] S. Lee, S. Shin, M. Kwon, K. Lee, B.C. De Cooman, Tensile Properties of Medium Mn Steel with a Bimodal UFG α + γ and Coarse δ-Ferrite Microstructure, Metall. Mater. Trans. A Phys. Metall. Mater. Sci. 48 (2017) 1678–1700. https://doi.org/10.1007/s11661-017-3979-z.

[6] J. Chiang, B. Lawrence, J.D. Boyd, A.K. Pilkey, Effect of microstructure on retained

austenite stability and work hardening of TRIP steels, Mater. Sci. Eng. A. 528 (2011) 4516–4521. https://doi.org/10.1016/j.msea.2011.02.032.

[7] J.G. Speer, B.C. De Cooman, D.K. Matlock, J.D. Schroth, Carbon partitioning into austenite after martensitic transformation, Acta Mater. 51 (2003) 2611–2622. https://doi.org/10.1016/S1359-6454(03)00059-4.

[8] E. de Moor, S. Lacroix, A.J. Clarke, J. Penning, J.G. Speer, Effect of retained austenite stabilized via quench and partitioning on the strain hardening of martensitic steels, Metall. Mater. Trans. A Phys. Metall. Mater. Sci. 39 (2008) 2586–2595. https://doi.org/10.1007/s11661-008-9609-z.

[9] E.J. Seo, L. Cho, Y. Estrin, B.C. De Cooman, Microstructure-mechanical properties relationships for quenching and partitioning (Q&P) processed steel, Acta Mater. 113 (2016) 124–139. https://doi.org/10.1016/j.actamat.2016.04.048.

[10] D. V. Edmonds, K. He, F.C. Rizzo, B.C. De Cooman, D.K. Matlock, J.G. Speer, Quenching and partitioning martensite-A novel steel heat treatment, Mater. Sci. Eng. A. 438–440 (2006) 25–34. https://doi.org/10.1016/j.msea.2006.02.133.

[11] M. Tumuluru, Effect of silicon and retained austenite on the liquid metal embrittlement cracking behavior of GEN3 and high-strength automotive steels, Weld. J. 98 (2019) 351S-364S. https://doi.org/10.29391/2019.98.029.

[12] J.W. Kim, S.P. Murugan, J.-H. Yoo, R. Ashiri, Y.-D. Park, Enhancing nugget size and weldable current range of ultra-high-strength steel using multi-pulse resistance spot welding, Https://Doi.Org/10.1080/13621718.2019.1680483. 25 (2019) 235–242.

https://doi.org/10.1080/13621718.2019.1680483.

[13] V.H. Baltazar Hernandez, S.S. Nayak, Y. Zhou, Tempering of martensite in dual-phase steels and its effects on softening behavior, Metall. Mater. Trans. A Phys. Metall. Mater. Sci. 42 (2011) 3115–3129. https://doi.org/10.1007/s11661-011-0739-3.

[14] M. Xia, E. Biro, Z. Tian, Y.N. Zhou, Effects of heat input and martensite on HAZ softening in laser welding of dual phase steels, ISIJ Int. 48 (2008) 809–814. https://doi.org/10.2355/isijinternational.48.809.

[15] Y. Lu, A. Peer, T. Abke, M. Kimchi, W. Zhang, Subcritical heat affected zone softening in hot-stamped boron steel during resistance spot welding, Mater. Des. 155 (2018) 170–184. https://doi.org/10.1016/j.matdes.2018.05.067.

[16] X.N. Wang, Q. Sun, Z. Zheng, H.S. Di, Microstructure and fracture behavior of laser welded joints of DP steels with different heat inputs, Mater. Sci. Eng. A. 699 (2017) 18–25. https://doi.org/10.1016/j.msea.2017.05.078.

[17] F. Hiroki, H. Kouichi, O. Toru, F. Hidetoshi, Welding International Effects of HAZ softening on the strength and elongation of resistance spot-welded joints in high-strength steel sheet in an in-plane tensile test Effects of HAZ softening on the strength and elongation of resistance spot-welded joints in high-strength steel sheet in an in-plane tensile test, (2018). https://doi.org/10.1080/01431161.2017.1346890.

[18] Z. Wu, S. Liu, Z. Yang, H. Zhou, E. Li, H. Pan, Y. Chen, L. Lu, L. Liu, Simultaneously improved the strength dramatically and eliminated HAZ softening of DP980 steel pulsed-arc welding joints by PWHT, Mater. Sci. Eng. A. 837 (2022).

https://doi.org/10.1016/J.MSEA.2022.142752.

[19] H. Ghassemi-Armaki, E. Biro, S. Sadagopan, Advanced Characterization of HAZ Softening of AHSS for Crash Modeling, ISIJ Int. 57 (2017) 1451–1460. https://doi.org/10.2355/isijinternational.ISIJINT-2016-649.

[20] V.H. Baltazar Hernandez, S.S. Nayak, Y. Zhou, Tempering of Martensite in Dual-Phase Steels and Its Effects on Softening Behavior, Metall. Mater. Trans. A 2011 4210. 42 (2011) 3115–3129. https://doi.org/10.1007/S11661-011-0739-3.

[21] M. Tamizi, M. Pouranvari, M. Movahedi, The Role of HAZ Softening on Cross-Tension Mechanical Performance of Martensitic Advanced High Strength Steel Resistance Spot Welds, Metall. Mater. Trans. A Phys. Metall. Mater. Sci. 52 (2021) 655–667. https://doi.org/10.1007/s11661-020-06104-5.

[22] T. Furuhara, K. Kobayashi, T. Maki, Control of cementite precipitation in lath martensite by rapid heating and tempering, ISIJ Int. 44 (2004) 1937–1944. https://doi.org/10.2355/isijinternational.44.1937.

[23] A. Nagao, K. Hayashi, K. Oi, S. Mitao, N. Shikanai, Refinement of Cementite in High Strength Steel Plates by Rapid Heating and Tempering, Mater. Sci. Forum. 539–543 (2007) 4720–4725. https://doi.org/10.4028/WWW.SCIENTIFIC.NET/MSF.539-543.4720.

[24] S.T. Ahn, D.S. Kim, W.J. Nam, Microstructural evolution and mechanical properties of low alloy steel tempered by induction heating, J. Mater. Process. Technol. 160 (2005) 54–58. https://doi.org/10.1016/J.JMATPROTEC.2004.03.019.

[25] D.C. Saha, S.S. Nayak, E. Biro, A.P. Gerlich, Y. Zhou, Mechanism of Secondary Hardening in Rapid Tempering of Dual-Phase Steel, Metall. Mater. Trans. A 2014 4513. 45 (2014) 6153–6162. https://doi.org/10.1007/S11661-014-2591-8.

[26] R.C. Thomson, M.K. Miller, Carbide precipitation in martensite during the early stages of tempering Cr- andMo-containing low alloy steels, Acta Mater. 46 (1998) 2203–2213. https://doi.org/10.1016/S1359-6454(97)00420-5.

[27] M. Jung, S.-J. Lee, Y.-K. Lee, Microstructural and Dilatational Changes during Tempering and Tempering Kinetics in Martensitic Medium-Carbon Steel, Metall. Mater. Trans. A 2009 403. 40 (2009) 551–559. https://doi.org/10.1007/S11661-008-9756-2.

[28] D.C. Saha, S.S. Nayak, E. Biro, A.P. Gerlich, Y. Zhou, Mechanism of Secondary Hardening in Rapid Tempering of Dual-Phase Steel, Metall. Mater. Trans. A Phys. Metall. Mater. Sci. 45 (2014) 6153–6162. https://doi.org/10.1007/s11661-014-2591-8.

[29] D.C. Saha, E. Biro, A.P. Gerlich, Y. Zhou, Influences of blocky retained austenite on the heat-affected zone softening of dual-phase steels, Mater. Lett. 264 (2020) 127368. https://doi.org/10.1016/j.matlet.2020.127368.

[30] K.A. Taylor, G.B. Olson, M. Cohen, J.B.V. Sande, Carbide precipitation during stage I tempering of Fe-Ni-C martensites, Metall. Trans. A. 20 (1989) 2749–2765. https://doi.org/10.1007/BF02670168.

[31] F.G. Caballero, C. García-Mateo, C.G. de Andrés, Dilatometric Study of Reaustenitisation of High Silicon Bainitic Steels: Decomposition of Retained Austenite, Mater. Trans. 46 (2005) 581–586. https://doi.org/10.2320/MATERTRANS.46.581.

[32] S. Nagakura, Y. Hirotsu, M. Kusunoki, T. Suzuki, Y. Nakamura, Crystallographic study of the tempering of martensitic carbon steel by electron microscopy and diffraction, Metall. Trans. A 1983 146. 14 (1983) 1025–1031. https://doi.org/10.1007/BF02670441.

[33] E. Biro, J.R. McDermid, S. Vignier, Y. Norman Zhou, Decoupling of the softening processes during rapid tempering of a martensitic steel, Mater. Sci. Eng. A. 615 (2014) 395–404. https://doi.org/10.1016/j.msea.2014.07.102.

[34] M. Xia, E. Biro, Z. Tian, Y.N. Zhou, Effects of heat input and martensite on HAZ softening in laser welding of dual phase steels, ISIJ Int. 48 (2008) 809–814. https://doi.org/10.2355/isijinternational.48.809.

[35] R.C. Thomson, M.K. Miller, Carbide precipitation in martensite during the early stages of tempering Cr- and Mo-containing low alloy steels, Acta Mater. 46 (1998) 2203–2213. https://doi.org/10.1016/S1359-6454(97)00420-5.

[36] Y. Zhang, D. Zhan, X. Qi, Z. Jiang, Austenite and precipitation in secondary-hardening ultra-high-strength stainless steel, Mater. Charact. 144 (2018) 393–399. https://doi.org/10.1016/J.MATCHAR.2018.07.038.

[37] N. Yurioka, T. Kasuya, Carbon Equivalent and Multiplying Factor for Hardenability of Steel, Weld. Res. Suppl. 6 (1993) 263–268. https://doi.org/https://app.aws.org/wj/supplement/WJ_1993_06_s263.pdf.

[38] AWS, AWS D8.1M:2007 Specification for Automotive Weld Quality-Resistance Spot Welding of Steel, 2007.

[39] M. Shojaee, C. Tolton, A.R.H. Midawi, C. Butcher, H. Ghassemi-Armaki, M. Worswick, E. Biro, Influence of loading orientation on mechanical properties of spot welds, Int. J. Mech. Sci. 224 (2022) 107327. https://doi.org/10.1016/J.IJMECSCI.2022.107327.

[40] ASTM, ASTM E384: Standard Test Method for Microindentation Hardness of Materials, Annu. B. ASTM Stand. (2016) 1–42. https://www.astm.org/Standards/E384 (accessed October 6, 2021).

[41] D.C. Ramachandran, S.D. Kim, J. Moon, C.H. Lee, J.H. Chung, E. Biro, Y. Do Park, Classification of martensite-austenite constituents according to its internal morphology in high-strength low alloy steel, Mater. Lett. 278 (2020). https://doi.org/10.1016/j.matlet.2020.128422.

[42] D.C. Ramachandran, J. Moon, C.-H. Lee, S.-D. Kim, J.-H. Chung, E. Biro, Y.-D. Park, Role of bainitic microstructures with M-A constituent on the toughness of an HSLA steel for seismic resistant structural applications, Mater. Sci. Eng. A. 801 (2021). https://doi.org/10.1016/j.msea.2020.140390.

[43] F. Peng, Y. Xu, X. Gu, Y. Wang, X. Liu, J. Li, The relationships of microstructure-mechanical properties in quenching and partitioning (Q&P) steel accompanied with microalloyed carbide precipitation, Mater. Sci. Eng. A. 723 (2018) 247–258. https://doi.org/10.1016/J.MSEA.2018.03.061.

[44] C. Song, H. Wang, Z. Sun, H. Yu, Analysis of precipitation characteristics of TiC at different quenching and partitioning temperatures and its effect on the mechanical properties, Mater. Sci. Eng. A. 824 (2021) 141868.

https://doi.org/10.1016/J.MSEA.2021.141868.

[45] M. Shamsujjoha, C.M. Enloe, A.C. Chuang, J.J. Coryell, H. Ghassemi-Armaki, Mechanisms of paint bake response in resistance spot-welded first and third generation AHSS, Materialia. 15 (2021) 100975. https://doi.org/10.1016/J.MTLA.2020.100975.

[46] D.C. Ramachandran, B. Figueredo, O. Sherepenko, W. Jin, Y. Do Park, E. Biro, A study on improving the mechanical performance by controlling the halo ring in the Q&P 980 steel resistance spot welds, J. Manuf. Process. 75 (2022) 320–330. https://doi.org/10.1016/j.jmapro.2022.01.019.

[47] E. Biro, S. Vignier, C. Kaczynski, J.R. McDermid, E. Lucas, J.D. Embury, Y.N. Zhou, Predicting transient softening in the sub-critical heat-affected zone of dual-phase and martensitic steel welds, ISIJ Int. 53 (2013) 110–118. https://doi.org/10.2355/isijinternational.53.110.

[48] E. Biro, J.R. McDermid, J.D. Embury, Y. Zhou, Softening kinetics in the subcritical heat-affected zone of dual-phase steel welds, Metall. Mater. Trans. A Phys. Metall. Mater. Sci. 41 (2010) 2348–2356. https://doi.org/10.1007/s11661-010-0323-2.

[49] O.T. Betiku, M. Shojaee, O. Sherepenko, A.R.H. Midawi, A.M. Chertov, H. Ghassemi-Armaki, R.G. Maev, E. Biro, Optimizing post-weld performance of press-hardened steel resistance spot welds by controlling fusion zone porosity, Weld. World. 1 (2022) 1–14. https://doi.org/10.1007/S40194-022-01332-2/FIGURES/15.

[50] J.H. Hollomon, L.D. Jaffe, Time-temperature relations in tempering steel, Trans. Am. Inst. Min. Metall. Eng. 162 (1945) 223–249.

[51] S.S. Nayak, V.H. Baltazar Hernandez, Y. Zhou, Effect of chemistry on nonisothermal tempering and softening of dual-phase steels, Metall. Mater. Trans. A Phys. Metall. Mater. Sci. 42 (2011) 3242–3248. https://doi.org/10.1007/s11661-011-0868-8.

[52] S. Vignier, E. Biro, M. Hervé, Predicting the hardness profile across resistance spot welds in martensitic steels, Weld. World. 58 (2014) 297–305. https://doi.org/10.1007/s40194-014-0116-0.

[53] J.W. Park, H.C. Lee, S. Lee, Composition, microstructure, hardness, and wear properties of high-speed steel rolls, Metall. Mater. Trans. A 1999 302. 30 (1999) 399–409. https://doi.org/10.1007/S11661-999-0329-9.

[54] H. Zhang, B. Dou, H. Tang, Y. He, S. Guo, Secondary hardening in laser rapidly solidified Fe68(MoWCrVCoNiAlCu)32 medium-entropy high-speed steel coatings, Mater. Des. 159 (2018) 224–231. https://doi.org/10.1016/J.MATDES.2018.08.050.

[55] Y.F. Shen, C.M. Wang, X. Sun, A micro-alloyed ferritic steel strengthened by nanoscale precipitates, Mater. Sci. Eng. A. 528 (2011) 8150–8156. https://doi.org/10.1016/J.MSEA.2011.07.065.

[56] J.H. Jang, I.G. Kim, H.K.D.H. Bhadeshia, Substitutional solution of silicon in cementite: A first-principles study, Comput. Mater. Sci. 44 (2009) 1319–1326. https://doi.org/10.1016/J.COMMATSCI.2008.08.022.

[57] T. Chen, Z. Ling, M. Wang, L. Kong, Effect of post-weld tempering pulse on microstructure and mechanical properties of resistance spot welding of Q&P1180 steel, Mater. Sci. Eng. A. 831 (2022). https://doi.org/10.1016/j.msea.2021.142164.

1

2